# Source-detector calibration in three-dimensional Bayesian optical diffusion tomography

Seungseok Oh*, Adam B. Milstein*, Rick P. Millane+,

Charles A. Bouman* and Kevin J. Webb*

* School of Electrical and Computer Engineering

Purdue University, West Lafayette, Indiana 47907-1285

+ Department of Electrical and Computer Engineering

University of Canterbury,

Private Bag 4800, Christchurch, New Zealand

*webb@ecn.purdue.edu*

Optical diffusion tomography is a method for reconstructing three-dimensional optical properties from light that passes through a highly scattering medium. Computing reconstructions from such data requires the solution of a nonlinear inverse problem. The situation is further complicated by the fact that while reconstruction algorithms typically assume exact knowledge of the optical source and detector coupling coefficients, these coupling coefficients are generally not available in practical measurement systems. A new method for estimating these unknown coupling coefficients in the three-dimensional reconstruction process is described. The joint problem of coefficient estimation and three-dimensional reconstruction is formulated in a Bayesian framework, and the resulting estimates are computed using a variation of iterative coordinate descent optimization that is adapted for this problem. Simulations show that this approach is an accurate and efficient method for simultaneous reconstruction of absorption and diffusion coefficients, as well as the coupling coefficients. A simple experimental result validates the approach. © 2002 Optical Society of America

## 1. Introduction

Optical diffusion tomography (ODT) is an imaging modality that has potential in applications such as medical imaging, environmental sensing, and non-destructive testing.[1] In this technique, measurements of the light that propagates through a highly scattering medium are used to recon-

struct the absorption and/or the scattering properties of the medium as a function of position. In highly scattering media such as tissue, the diffusion approximation to the transport equations is sufficiently accurate and provides a computationally tractable forward model. However, the inverse problem of reconstructing the absorption and/or scattering coefficients from measurements of the scattered light is highly nonlinear. This nonlinear inverse problem can be very computationally expensive, so methods that reduce the computational burden are of critical importance.[2–6]

Another important issue for practical ODT imaging, that is addressed in this paper, is accurate modeling of the source and detector coupling coefficients.[7] These coupling coefficients determine weights for sources and detectors in a diffusion equation model for the scattering domain. The physical source of the source/detector coupling variability is associated with the optical components external to the scattering domain, for example, the placement of fibers, the variability in switches, etc. Variations in the coupling coefficients can result in severe, systematic reconstruction distortions. In spite of its practical importance, this issue has received little attention.

Two preprocessing methods have been investigated to correct for source/detector coupling errors before inversion. Jiang *et al.*[8,9] calibrated coupling coefficients and a boundary coefficient by comparing prior measurements of photon flux density for a homogeneous medium with the corresponding computed values. This scheme has been applied in clinical studies.[10–12] This method of calibration requires a set of reference measurements from a homogeneous sample, in addition to the measurements used to reconstruct the inhomogeneous image. Iftimia *et al.*[13] proposed a preprocessing scheme that involved minimization of the mean square error between the measurements for the given inhomogeneous phantom and the computed values with an assumed homogeneous medium. However, although this approach does not require prior homogeneous reference measurements, it neglects the influence of an inhomogeneous domain when determining the source and detector weights.

In order to reconstruct the image from a single set of measurements from the domain to be imaged, it is necessary to estimate the coupling coefficients as the image is reconstructed. For example, Boas *et al.*[7] proposed a scheme for estimating individual coupling coefficients as part of the reconstruction process. They simultaneously estimated both absorption and coupling coefficients by formulating a linear system which consisted of the perturbations of the measurements in a Rytov approximation and the logarithms of the source and detector coupling coefficients. No results have been reported for nonlinear reconstruction of both absorption and diffusion images, and the individual coupling coefficients.

In this paper, we describe an efficient algorithm for estimating individual source and detector coupling coefficients as part of the reconstruction process for both absorption and diffusion images. This approach is based on the formulation of our problem in a unified Bayesian regularization framework containing terms for both the unknown 3-D optical properties and the coupling coefficients. The resulting cost function is then jointly minimized to both reconstruct the image and estimate the needed coefficients. To perform this minimization, we adapt our iterative coordinate decent optimization method[2] to include closed form steps for the update of the coupling coefficient estimates. This unified optimization approach results in an algorithm which can reconstruct images and estimate the coupling coefficients without the need for prior calibration. In a previous experiment, we used the algorithm to effectively estimate a single coefficient from a measured 3-D data set.[14] Simulation results show that our method can substantially improve reconstruction quality even when there are a large number of severely non-uniform coupling coefficients. Our approach is applied to a simple phantom experiment.

## 2. Problem Formulation

In a highly scattering medium with low absorption, such as soft tissue in the 650-1300 nm wavelength range, the photon flux density is accurately modeled by the diffusion equation.[15, 16] In

4

frequency domain optical diffusion imaging, the light source is amplitude modulated at angular frequency $\omega$, and the complex modulation envelope of the optical flux density is measured at the detectors. The complex amplitude $\phi_k(r)$ of the modulation envelope due to a point source at position $a_k$ satisfies the frequency domain diffusion equation

$$\nabla \cdot [D(r)\nabla\phi_k(r)] + [-\mu_a(r) - j\omega/c]\,\phi_k(r) = -\delta(r - a_k), \tag{1}$$

where $r$ is position, $c$ is the speed of light in the medium, $D(r)$ is the diffusion coefficient, and $\mu_a(r)$ is the absorption coefficient. We consider a region to be imaged that is surrounded by $K$ point sources at positions $a_k$, for $1 \le k \le K$, and $M$ detectors at positions $b_m$, for $1 \le m \le M$. The 3-D domain is discretized into $N$ grid points, denoted by $r_1, \cdots, r_N$. The unknown image is then represented by a $2N$ dimensional column vector $x$ containing the absorption and diffusion coefficients at each discrete grid point

$$x = [\mu_a(r_1), \ldots, \mu_a(r_N), D(r_1), \ldots, D(r_N)]^t\,. \tag{2}$$

We will use the notation $\phi_k(r; x)$ in place of $\phi_k(r)$, in order to emphasize the dependence of the solution to (1) on the unknown material properties $x$.

Let $y_{km}$ be the complex measurement at detector location $b_m$ and using a source at location $a_k$. This measurement is a sample of a random variable $Y_{km}$, which we will model as a sum of the true signal and Gaussian noise. The datum mean value of $Y_{km}$ is given by

$$E[Y_{km}|x, s_k, d_m] = s_k d_m \phi_k(b_m; x)\,, \tag{3}$$

where $\phi_k(b_m; x)$ is the solution of (1) evaluated at position $b_m$; $s_k$ and $d_m$ are complex constants representing the unknown source and detector distortions; and $E[\cdot|x, s_k, d_m]$ denotes the conditional expectation given $x$, $s_k$, and $d_m$. [1]

_____

[1]We assume that the physical sources and detectors provide an adequate measure of $\phi$, that they do not perturb the diffusion equation solution, and that they have an equivalent point representation.

Our objective is to simultaneously estimate the unknown image $x$ together with the unknown source and detector coupling coefficient vectors $s = [s_1, s_2, \ldots, s_K]^t$ and $d = [d_1, d_2, \ldots, d_M]^t$. The coupling coefficients are different for different sources and detectors, and are not known *a priori*. In general, the values of $s_k$ and $d_m$ will vary in both amplitude and phase for real physical systems. Typically, amplitude variations can be caused by different excitation intensities for the sources and different collection efficiencies for the detectors, and phase variation can be caused by the different effective positions of the sources and detectors. Without these parameter vectors, accurate reconstruction of $x$ is not possible.

The measurement vector $y$ is formed by raster ordering the measurements $y_{km}$ in the form

$$y = [y_{11}, \ldots, y_{1M}, y_{21}, \ldots, y_{2M}, \ldots, y_{KM}]^t . \tag{4}$$

The conditional expectation of $Y = [Y_{11}, \ldots, Y_{1M}, Y_{21}, \ldots, Y_{2M}, \ldots, Y_{KM}]^t$ is then given by

$$E[Y|x, s, d] = \text{diag}(s \otimes d)\Phi(x) , \tag{5}$$

where $s \otimes d$ is the Kronecker product of $s$ and $d$, $\text{diag}(w)$ is a diagonal matrix whose $(i,i)$-th element is equal to the $i$-th element of the vector $w$, and $\Phi(x)$ is the corresponding raster order of the values $\phi_k(b_m; x)$ given by

$$\Phi(x) = [\ \phi_1(b_1; x), \phi_1(b_2; x), \ldots, \phi_1(b_M; x), \phi_2(b_1; x), \ldots, \phi_K(b_M; x)\ ]^t . \tag{6}$$

In order to simplify notation, we define the forward model vector $f(x, s, d)$ as

$$f(x, s, d) = \text{diag}(s \otimes d)\Phi(x) . \tag{7}$$

We use a shot noise model for the detector noise.[2, 17] The shot noise model assumes independent noise measurements that are Gaussian with variance proportional to the signal amplitude. This results in the following expression for the conditional density of $Y$

$$p(y|x, s, d, \alpha) = \frac{1}{(\pi\alpha)^P |\Lambda|^{-1}} \exp\left[-\frac{||y - f(x, s, d)||_\Lambda^2}{\alpha}\right], \tag{8}$$

6

where $P = KM$ is the number of measurements, $\alpha$ is an unknown parameter that scales the noise variance, $\Lambda = \text{diag}([1/|y_{11}|, \ldots, 1/|y_{1M}|, 1/|y_{21}|, \ldots, 1/|y_{KM}|]^t)$, and $||w||_{\Lambda}^2 = w^H \Lambda w$.

We determine $x$, $s$, $d$, and $\alpha$ from the measurements $y$. Because this is an ill-posed inverse problem, we employ a Bayesian framework to incorporate a prior model for $x$, the image.[2] We then maximize the posterior probability of $x$ jointly with respect to $y$, $s$, $d$, and $\alpha$. This yields the estimators

$$
\begin{aligned}
(\hat{x}_{MAP}, \hat{s}, \hat{d}, \hat{\alpha}) &= \arg \max_{(x \geq 0, s, d, \alpha)} \{ \log p(x|y, s, d, \alpha) \} \\
&= \arg \max_{(x \geq 0, s, d, \alpha)} \{ \log p(y|x, s, d, \alpha) + \log p(x) \} ,
\end{aligned}
\tag{9}
$$

where $p(y|x, s, d, \alpha)$ is the data likelihood, and $p(x)$ is the prior model for the image. The estimate $\hat{x}_{MAP}$ is essentially the maximum *a posteriori* (MAP) estimate of the image, but it is computed by simultaneously optimizing with respect to the unknown parameters $s$, $d$, and $\alpha$. Quantities such as $s$, $d$, and $\alpha$ are sometimes known as nuisance parameters, because they are not of direct interest, but are required for accurate estimation of the desired quantity $x$. A variety of methods have been proposed for estimating such parameters. These methods range from true maximum likelihood estimation using Monte Carlo Markov chain (MCMC) techniques,[18–20] to joint MAP estimation of the unknown image and parameters.[21,22] Our method is a form of joint MAP estimation, but with a uniform (i.e., improper) prior distribution for $s$, $d$, and $\alpha$. It is worth noting that such estimators can behave poorly in certain cases.[23] However, when the number of measurements is large compared to the dimensionality of the unknowns, as in our case for $s$, $d$, and $\alpha$, these estimators generally work well.

We use the generalized Gaussian Markov random field (GGMRF) prior model[24] for the image $x$,

$$
p(x) = p([\mu_a(r_1), \mu_a(r_2), \ldots, \mu_a(r_N)]^T) \cdot p([D(r_1), D(r_2), \ldots, D(r_N)]^T)
$$

$$= \left[ \frac{1}{\sigma_0{}^N z(p_0)} \exp\left\{ -\frac{1}{p_0 \sigma_0{}^{p_0}} \sum_{\{i,j\}\in\mathcal{N}} b_{0,i-j}|x_i - x_j|^{p_0} \right\} \right]$$

$$\cdot \left[ \frac{1}{\sigma_1{}^N z(p_1)} \exp\left\{ -\frac{1}{p_1 \sigma_1{}^{p_1}} \sum_{\{i,j\}\in\mathcal{N}} b_{1,i-j}|x_{N+i} - x_{N+j}|^{p_1} \right\} \right]$$

$$= \prod_{u=0}^{1} \left[ \frac{1}{\sigma_u{}^N z(p_u)} \exp\left\{ -\frac{1}{p_u \sigma_u{}^{p_u}} \sum_{\{i,j\}\in\mathcal{N}} b_{u,i-j}|x_{uN+i} - x_{uN+j}|^{p_u} \right\} \right] , \qquad (10)$$

where $\sigma_0$ and $\sigma_1$ are normalization parameters for $\mu_a$ and $D$, respectively, and $1 \le p_0 \le 2$ and $1 \le p_1 \le 2$ control the degree of edge smoothness for $\mu_a$ and $D$, respectively. The set $\mathcal{N}$ consists of all pairs of adjacent grid points, $z(p_0)$ and $z(p_0)$ are normalization constants, and $b_{0,i-j}$ and $b_{1,i-j}$ represent the coefficients assigned to neighbors $i$ and $j$ for $\mu_a$ and $D$, respectively. This prior model enforces smoothness in the solution while preserving sharp edge transitions, and its effectiveness for this kind of problem has been shown previously.[2]

## 3. Optimization

Let $c(x, s, d, \alpha)$ denote the cost function to be minimized in (9). Then using the models of (8) and (10) and removing constant terms results in

$$c(x, s, d, \alpha) = \frac{1}{\alpha}||y - f(x, s, d)||_\Lambda^2 + P \log \alpha + \sum_{u=0}^{1} \frac{1}{p_u \sigma_u{}^{p_u}} \sum_{\{i,j\}\in\mathcal{N}} b_{u,i-j}|x_{uN+i} - x_{uN+j}|^{p_u}. \quad (11)$$

The objective is then to compute

$$(\hat{x}_{MAP}, \hat{s}, \hat{d}, \hat{\alpha}) = \arg \min_{(x\ge 0, s, d, \alpha)} c(x, s, d, \alpha) . \qquad (12)$$

To solve this problem, we adapt the iterative coordinate decent (ICD) method.[2] The ICD method works by sequentially updating parameters of the optimization, so that each update monotonically reduces the cost function. Previous implementations of ICD sequentially updated pixels in the vector $x$. Here we generalize the ICD method so that the parameters $s$, $d$, and $\alpha$ are also included in the sequence of updates. More specifically, in each iteration of the ICD algorithm, $s$, $d$, $\alpha$, and

$x$ are updated sequentially using the relations

$$\hat{\alpha} \quad \leftarrow \quad \arg\min_{\alpha} \; c(\hat{x}, \hat{s}, \hat{d}, \alpha) \tag{13}$$

$$\hat{s} \quad \leftarrow \quad \arg\min_{s} \; c(\hat{x}, s, \hat{d}, \hat{\alpha}) \tag{14}$$

$$\hat{d} \quad \leftarrow \quad \arg\min_{d} \; c(\hat{x}, \hat{s}, d, \hat{\alpha}) \tag{15}$$

$$\hat{x} \quad \leftarrow \quad ICD\_update_x \left\{ c(x, \hat{s}, \hat{d}, \hat{\alpha}), \hat{x} \right\} \tag{16}$$

where the $ICD\_update_x$ operation performs one iteration of ICD optimization to reduce the cost function $c(\cdot, \hat{s}, \hat{d}, \hat{\alpha})$ starting at the initial value $\hat{x}$. The result of $ICD\_update_x$ is then used to update the value of $\hat{x}$. Iterative application of these update equations produces a convergent sequence of deceasing costs.

The updates of (13), (14), and (15) can be calculated in closed form by setting the partial derivative with respect to each variable to zero and solving the resulting equations to yield

$$\hat{\alpha} \quad \leftarrow \quad \frac{1}{P} \; \| \; y - f(\hat{x}, \hat{s}, \hat{d}) \; \|_{\Lambda}^2 \tag{17}$$

$$\hat{s}_k \quad \leftarrow \quad \frac{[ \; \mathrm{diag}(\hat{d}) \; \Phi_k^{(s)}(\hat{x}) \; ]^H \Lambda_k^{(s)} \; y}{\| \; \mathrm{diag}(\hat{d}) \; \Phi_k^{(s)}(\hat{x}) \; \|_{\Lambda_k^{(s)}}^2} \qquad k = 1, 2, \ldots, K \tag{18}$$

$$\hat{d}_m \quad \leftarrow \quad \frac{[ \; \mathrm{diag}(\hat{s}) \; \Phi_m^{(d)}(\hat{x}) \; ]^H \Lambda_m^{(d)} \; y}{\| \; \mathrm{diag}(\hat{s}) \; \Phi_m^{(d)}(\hat{x}) \; \|_{\Lambda_m^{(d)}}^2} \qquad m = 1, 2, \ldots, M, \tag{19}$$

where $H$ denotes the Hermitian transpose, $\Lambda_k^{(s)} = \mathrm{diag}( \; [ \; 1/|y_{k1}|, 1/|y_{k2}|, \ldots, 1/|y_{kM}| \; ]^t \; )$ and $\Lambda_m^{(d)} = \mathrm{diag}( \; [ \; 1/|y_{1m}|, 1/|y_{2m}|, \ldots, 1/|y_{Km}| \; ]^t \; )$ are the inverse diagonal covariance matrices associated with source $k$ and detector $m$, respectively, and $\Phi_k^{(s)}(\hat{x}) = [ \; \phi_k(b_1; \hat{x}), \phi_k(b_2; \hat{x}), \ldots, \phi_k(b_M; \hat{x}) \; ]^t$ and $\Phi_m^{(d)}(\hat{x}) = [ \; \phi_1(b_m; \hat{x}), \phi_2(b_m; \hat{x}), \ldots, \phi_K(b_m; \hat{x}) \; ]^t$ are the complex amplitude vectors associated with source $k$ and detector $m$, respectively.

The update of the variable $x$ in (16) is of course more difficult since $x$ is a high dimensional vector, particularly in the 3-D case. To update the image, we use one scan of the ICD algorithm as an $ICD\_update_x$ operation. One ICD scan involves sequentially updating each element of $x$

with random ordering, and incorporation of the updated elements as the scan progresses. During this scan each element of $x$ is updated only once. At the beginning of an ICD scan, the nonlinear functional $f(x, s, d)$ is first expressed using a Taylor expansion as

$$||y - f(x, s, d)||_\Lambda^2 \simeq ||y - f(\hat{x}, \hat{s}, \hat{d}) - f'(\hat{x}, \hat{s}, \hat{d})\Delta x||_\Lambda^2 , \tag{20}$$

where $\Delta x = x - \hat{x}$, and $f'(\hat{x}, \hat{s}, \hat{d})$ represents the Fréchet derivative of $f(x, \hat{s}, \hat{d})$ with respect to $x$ at $x = \hat{x}$. Using (20), an approximate cost function for the original problem is

$$c(x, \hat{s}, \hat{d}, \hat{\alpha}) \simeq \frac{1}{\hat{\alpha}}||z - f'(\hat{x}, \hat{s}, \hat{d})x||_\Lambda^2 + \sum_{u=0}^{1} \frac{1}{p_u \sigma_u^{p_u}} \sum_{\{i,j\} \in \mathcal{N}} b_{u,i-j}|x_{uN+i} - x_{uN+j}|^{p_u} , \tag{21}$$

where

$$z = y - f(\hat{x}, \hat{s}, \hat{d}) + f'(\hat{x}, \hat{s}, \hat{d})\hat{x} . \tag{22}$$

Then, with the other image elements fixed, the ICD update for $\hat{x}_{uN+i}$ is given by

$$\hat{x}_{uN+i} \leftarrow \arg \min_{x_{uN+i} \geq 0} \left\{ \frac{1}{\hat{\alpha}} \left\| y - f(\hat{x}, \hat{s}, \hat{d}) - \left[ f'(\hat{x}, \hat{s}, \hat{d}) \right]_{*(uN+i)} (x_{uN+i} - \hat{x}_{uN+i}) \right\|_\Lambda^2 \right.$$
$$\left. + \frac{1}{p_u \sigma^{p_u}} \sum_{j \in \mathcal{N}_i} b_{u,i-j}|x_{uN+i} - \hat{x}_{uN+j}|^{p_u} \right\} , \tag{23}$$

where $[f'(\hat{x}, \hat{s}, \hat{d})]_{*(uN+i)}$ is the $(uN + i)$-th column of Fréchet matrix, and $\mathcal{N}_i$ is the set of grid points neighboring grid point $i$. To compute the solution to (23), we express the first term as a quadratic function of $x_{uN+i}$ and then perform a one-dimensional minimization that is solved by a half-interval search for the root of the analytical derivative.[2]

The Fréchet derivative $f'(\hat{x}, \hat{s}, \hat{d})$ is a $P \times 2N$ complex matrix given by

$$
f'(\hat{x}, \hat{s}, \hat{d}) = 
\begin{bmatrix}
\frac{\partial f_{11}(\hat{x},\hat{s}_1,\hat{d}_1)}{\partial \mu_a(r_1)} & \cdots & \frac{\partial f_{11}(\hat{x},\hat{s}_1,\hat{d}_1)}{\partial \mu_a(r_N)} & \frac{\partial f_{11}(\hat{x},\hat{s}_1,\hat{d}_1)}{\partial D(r_1)} & \cdots & \frac{\partial f_{11}(\hat{x},\hat{s}_1,\hat{d}_1)}{\partial D(r_N)} \\[8pt]
\frac{\partial f_{12}(\hat{x},\hat{s}_1,\hat{d}_2)}{\partial \mu_a(r_1)} & \cdots & \frac{\partial f_{12}(\hat{x},\hat{s}_1,\hat{d}_2)}{\partial \mu_a(r_N)} & \frac{\partial f_{12}(\hat{x},\hat{s}_1,\hat{d}_2)}{\partial D(r_1)} & \cdots & \frac{\partial f_{12}(\hat{x},\hat{s}_1,\hat{d}_2)}{\partial D(r_N)} \\[8pt]
\vdots & \ddots & \vdots & \vdots & \ddots & \vdots \\[8pt]
\frac{\partial f_{1M}(\hat{x},\hat{s}_1,\hat{d}_M)}{\partial \mu_a(r_1)} & \cdots & \frac{\partial f_{1M}(\hat{x},\hat{s}_1,\hat{d}_M)}{\partial \mu_a(r_N)} & \frac{\partial f_{1M}(\hat{x},\hat{s}_1,\hat{d}_M)}{\partial D(r_1)} & \cdots & \frac{\partial f_{1M}(\hat{x},\hat{s}_1,\hat{d}_M)}{\partial D(r_N)} \\[8pt]
\frac{\partial f_{21}(\hat{x},\hat{s}_2,\hat{d}_1)}{\partial \mu_a(r_1)} & \cdots & \frac{\partial f_{21}(\hat{x},\hat{s}_2,\hat{d}_1)}{\partial \mu_a(r_N)} & \frac{\partial f_{21}(\hat{x},\hat{s}_2,\hat{d}_1)}{\partial D(r_1)} & \cdots & \frac{\partial f_{21}(\hat{x},\hat{s}_2,\hat{d}_1)}{\partial D(r_N)} \\[8pt]
\vdots & \ddots & \vdots & \vdots & \ddots & \vdots \\[8pt]
\frac{\partial f_{KM}(\hat{x},\hat{s}_K,\hat{d}_M)}{\partial \mu_a(r_1)} & \cdots & \frac{\partial f_{KM}(\hat{x},\hat{s}_K,\hat{d}_M)}{\partial \mu_a(r_N)} & \frac{\partial f_{KM}(\hat{x},\hat{s}_K,\hat{d}_M)}{\partial D(r_1)} & \cdots & \frac{\partial f_{KM}(\hat{x},\hat{s}_K,\hat{d}_M)}{\partial D(r_N)}
\end{bmatrix},
\tag{24}
$$

where the first $N$ columns correspond to the $\mu_a$ components of $x$ and the remaining $N$ columns correspond to the $D$ components. In a similar manner to the Fréchet derivative commonly used for unity coupling coefficients,[25] it can be shown that each element of the matrix is given by

$$
\frac{\partial f_{km}(\hat{x}, \hat{s}_k, \hat{d}_m)}{\partial \mu_a(r_i)} = -\hat{s}_k \hat{d}_m g(b_m, r_i; \hat{x}) \phi_k(r_i; \hat{x}) A
\tag{25}
$$

$$
\frac{\partial f_{km}(\hat{x}, \hat{s}_k, \hat{d}_m)}{\partial D(r_i)} = -\hat{s}_k \hat{d}_m \nabla g(b_m, r_i; \hat{x}) \cdot \nabla \phi_k(r_i; \hat{x}) A \ ,
\tag{26}
$$

where $A$ is the voxel volume, the Green's function $g(b_m, r_i; \hat{x})$ is the solution of (1) for a point source located at $b_m$ (i.e., by setting $a_k \leftarrow b_m$ in (1), using reciprocity to reduce computation[25]) and a given image $\hat{x}$, $\nabla$ is the gradient operator with respect to $r_i$, and domain discretization errors are ignored. Note that the Fréchet derivative is the product of the coupling coefficient terms $\hat{s}_k \hat{d}_m$ and the derivative of $\phi_k(b_m; \hat{x})$ with respect to the optical parameter at that grid point. Thus, if the coupling coefficients are not accurately estimated, the formulas (25) and (26) do not yield accurate Fréchet derivatives, and thus the computed gradient direction of the cost function in (12) is not accurate. Therefore, accurate estimation of the coupling coefficients is essential for the ICD-Born iteration scheme.

The dimensions of the Fréchet derivative matrix are very large for practical 3-D imaging. For example, $(KM \times 2N \times 8) = 790$ MBytes of memory are needed to store the Fréchet derivative matrix for 30 sources, 48 detectors and a $33 \times 33 \times 33$ grid point image, if 4 bytes are used for a real number. However, the storage can be reduced by exploiting two facts. First, only the $(uN+i)$-th column of the Fréchet derivative matrix is needed to update $x_{uN+i}$, as seen in (23). Second, the Fréchet derivative in (25) and (26) is separable into the $\phi_k(r_i; \hat{x})$ term and the $g(b_m, r_i; \hat{x})$ term. Thus, we compute only $\phi_k(\cdot; \hat{x})$ for $k = 1, 2, \ldots, K$ and $g(b_m, \cdot; \hat{x})$ for $m = 1, 2, \ldots, M$ before the ICD update of the whole image, and then when $x_i$ is updated the $i$-th column of the Fréchet derivative is computed using these vectors. This method, which involves storing the forward solutions for all sources, the Green's function for all detectors, and only one column of the Fréchet derivative matrix, reduces the required memory to $(KN + MN + KM) \times 8$ bytes without requiring additional computation. In the above example, the required memory is then only 22 MBytes. Note that this implementation differs from the work of Ye, $et\ al.$,[2,3] where they did not need consider this storage issue because they dealt with a two-dimensional problem. The whole optimization procedure is summarized in the pseudo-code of Fig. 1.

## 4. Results

### A. Simulation

The performance of the algorithm described above was investigated by simulation using cubic tissue phantoms of dimension $8 \times 8 \times 8$ cm on an edge and with background $D = 0.03$ cm and $\mu_a = 0.02$ cm$^{-1}$. Two phantoms were used. Phantom A has two spherical $\mu_a$ inhomogeneities with diameters of 2.25 cm and 2.75 cm and central values of 0.070 cm$^{-1}$ that decay smoothly as a fourth order polynomial to the background value, and two spherical $D$ inhomogeneities with diameters of 2.25 cm and a central value of 0.01 cm that increase smoothly to the background value as a fourth order polynomial. Phantom A is shown as an isosurface plot in Fig. 2(a,b), and as gray scale plots

of cross-sections in Fig. 3(a,b). Phantom B has a high absorption inhomogeneity with a peak value of $\mu_a = 0.07$ cm$^{-1}$ near one face of the cube and a low diffusion inhomogeneity near the center with a diameter of 2.75 cm and a central value of 0.01 cm that increases smoothly as a fourth order polynomial to the background value, as shown in Fig. 4(a,b) and Fig. 5(a,b). Phantom B was used to assess whether an absorber close to a set of sources and detectors is difficult to reconstruct, since its effect might be compensated for by reduced source and detector coupling coefficients. Five sources, with a modulation frequency of 100 MHz, and eight detectors are located on each face (Fig. 6a), yielding $K = 30$ and $M = 48$. Shot noise was added to the data, and the average signal-to-noise ratio for sources and detectors on opposite faces was 33 dB. The complex source/detector coupling coefficients (a total of 78 parameters) were generated with a Gaussian distribution centered at $1 + 0i$ and having a standard deviation of $\frac{\sigma_{\text{coeff}}}{\sqrt{2}}(1 + i)$, with $\sigma_{\text{coeff}} = 0.5$ (Fig. 7a). The domain was discretized onto $33 \times 33 \times 33$ grid points, and the forward model (1) solved using finite differences. Referring to Fig. 6(b), a zero-flux ($\phi = 0$) boundary condition on the outer boundary provides the approximate boundary condition on the physical boundary.[2,17] The sources and detectors were placed 0.6 grid points in from the zero-flux boundary, achieved through appropriate weighting of the nearest grid points. Only nodes within the imaging boundary were updated, which excludes the three outermost layers of grid points, to avoid singularities near the sources and detectors. The optimization was initialized using the homogeneous values $D = 0.03$ cm and $\mu_a = 0.02$ cm$^{-1}$. The image prior model used $p_0 = 2.0$, $\sigma_0 = 0.01$ cm$^{-1}$, $p_1 = 2.0$, and $\sigma_1 = 0.004$ cm.

Reconstructions of $\mu_a$ and $D$ after 30 iterations are shown in Fig. 2(c,d) and Fig. 4(c,d), for Phantom A, and in Fig. 3(c,d) and Fig. 5(c,d) for Phantom B. The corresponding images reconstructed with the correct values of coupling coefficients are shown for comparison in Fig. 2(e,f), Fig. 4(e,f), Fig. 3(e,f), and Fig. 5(e,f). Our algorithm reconstructs images quite similar to those reconstructed when the true values of the coupling coefficients are used. The corresponding im-

ages reconstructed with all coupling coefficients set to $1 + 0i$ are shown in Fig. 2(g,h), Fig. 4(g,h), Fig. 3(g,h) and Fig. 5(g,h). These show that poor reconstructions are obtained if the source and detector coupling is not accounted for in the reconstruction process. This is due to the effectively incorrect forward model and hence incorrect Fréchet derivatives. In fact, for the large range of source and detector coupling coefficients used in these examples, the images reconstructed without calibration differ little from the initial starting point of the optimization, when the coupling coefficients are fixed at $1 + 0i$. The convergence of the normalized root mean square error (NRMSE) between the phantoms and the reconstructed images is shown in Fig. 8. The NRMSE is defined by

$$\text{NRMSE} \quad = \quad \left[ \frac{1}{2} \sum_{u=0}^{1} \frac{\sum_{r_i \in R} |\hat{x}_{uN+i} - x_{uN+i}|^2}{\sum_{r_i \in R} |x_{uN+i}|^2} \right]^{1/2}, \tag{27}$$

where $R$ is the set of the updated grid points within the imaging boundary (shown in Fig. 6(b)), $\hat{x}_{uN+i}$ is the reconstructed value of $(uN + i)$-th image element, and $x_{uN+i}$ is the correct value. The NRMSE obtained with the reconstruction incorporating calibration is similar to that obtained when the correct coupling coefficients are used. However, if calibration is not used, there is little decrease in the NRMSE from the starting value.

The accuracy of the estimated coupling coefficients is shown in Fig. 7(b,c), where the differences between the true coupling coefficients and those estimated after 30 iterations is given. The NRMSE error after 30 iterations is 0.011 for Phantom A and 0.017 for Phantom B, which are only 2% and 3% of the standard deviation of the coupling coefficients, respectively, indicating accurate recovery. Figure 9 shows the variation of the NRMSE error between the estimated and true coupling coefficients versus iteration, showing good convergence in only a few iterations. The results therefore indicate that our algorithm reconstructs accurate images without prior calibration by the estimation of the coupling coefficients in an efficient optimization scheme.

For Phantom B, the absorber close to one source-detector plane is reconstructed quite accurately and is not distorted by the variable coupling coefficients of the sources and detectors. Some

14

small spikes of low $\mu_a$ appear in the neighborhood of some of the sources and detectors (Fig. 5(b)), as noted previously,[7] but the effect is quite small. However, the final NRMSE is somewhat larger for Phantom B than for Phantom A (Fig. 8), and the real part of some of the coupling coefficients is underestimated (Fig. 7(c)). We categorize the sources and detectors on the side nearest the absorber as Group 1, and the remainder as Group 2. Most of the underestimated coefficients are those for sources and detectors on the face close to the absorber. The estimation error for these coupling coefficients (Group 1) is larger than the remaining sources and detectors (Fig. 9(b)). Therefore, because the light transmitted through the absorber is highly attenuated, it is partially compensated for by reduced estimated coupling coefficients. As noted above, however, the effect is quite small.

In order to study the effect of the variability of the coupling coefficients, reconstructions were performed for Phantom A for different standard deviations of the (real and imaginary parts of the) coupling coefficients, $\sigma_{\text{coeff}}$. The coupling coefficients were generated with a Gaussian distribution centered at $1 + 0i$ and having $\frac{\sigma_{coeff}}{\sqrt{2}}(1 + i)$, and images are the reconstructed results after 30 iterations of our algorithm. The image NRMSE is compared for various standard derivations in Fig. 10. Estimating the calibration coefficients reduces the NRMSE, as expected. The error without calibration did not increase beyond about 0.28 with increasing $\sigma_{\text{coeff}}$, as this value for the image NRMSE corresponds to the initial value with the correct background parameters and indicates that an image is not recovered. To establish the gradual deterioration of the image with source-detector coupling coefficients that are not accounted for in the reconstruction, Fig. 11(a,b) shows the image obtained with for $\sigma_{\text{coeff}} = 0.02$ and Fig. 11(c,d) that for $\sigma_{\text{coeff}} = 0.04$, as compared with the true images in Fig. 3(a,b). This result indicates that accurate estimation of the coupling coefficients is crucial for determining accurate images. The $\sigma_{\text{coeff}}$ will obviously be a function of the specific experimental arrangement. Figure 10 serves as an illustration of the impact of variations in the source-detector coupling. While some experimental arrangements may have (approximately) a

single, scalar source-detector weight,[14] it is still important to determine this value.

We have established that multi-resolution techniques such as multigrid achieve more reliable convergence of the cost function while dramatically reducing the computation time in two-dimensional optical diffusion tomography.[3] The approach presented for extracting the source-detector weights as part of the image reconstruction in a Bayesian framework could be extended to multi-resolution approaches. We investigated a simple multi-resolution approach by using a coarse grid solution ($17 \times 17 \times 17$) to initialize a fine grid solution ($33 \times 33 \times 33$). Better convergence was achieved using this simple two-grid approach with various initial conditions consisting of uniform $D$ and $\mu_a$ differing from the true background by as much as a factor of three. This performance improvement occurs both with known and estimated source-detector weights. Also, we noticed that in some cases with a fixed, fine grid, the cost function with variable source-detector weights was slightly larger than that with the true weights set. While the images in these cases were still excellent, the additional degrees of freedom should have resulted in a smaller value of the cost function. Using the multi-resolution approach, this was indeed the case, providing further evidence of the robustness of our approach. We emphasize that the algorithm we present for extraction of the source-detector weights in a Bayesian framework was consistently effective, regardless of the particular iterative reconstruction approach.

## B. Experiment

The effectiveness of our source-detector calibration approach was evaluated for measurements made on an optically clear culture flask containing a black plastic cylinder embedded in a turbid suspension (Fig. 12(a)). The plastic cylinder was embedded in a 0.5% concentration of Intralipid solution. The data was collected with an inexpensive apparatus comprised of an infrared LED operating at 890 nm and a silicon p-i-n photodiode, as schematically depicted in Fig. 12(b). With the source centrally located, as shown in Fig. 12(b), the detector located on the other side of the flask was

mechanically scanned in the same plane as the source, and data were taken at 25 symmetrical locations. The flask was rotated, so that the relative positions of source and detector were reversed, and another set of data taken. This resulted in a total of two source positions with 25 detector measurements each. The sources were modulated at 50 MHz.

For this experiment, there are a total of two unknown calibration parameters to be estimated. Each set of 25 measurements used a single detector; so we modeled all 25 measurements with a single detector calibration parameter. Without loss of generality, the two source calibration parameters were assumed to be 1 since, for this experiment, any change in source phase and amplitude can be equivalently accounted for by the detector calibration parameters.

Inversions were performed for the absorption coefficients and coupling coefficients, assuming $D$ known. The domain was discretized into $65 \times 33 \times 65$ grid points. For computational efficiency, we used a simple multiresolution technique in which 200 coarser grid ($33 \times 17 \times 33$) iterations are followed by 30 fine grid iterations. We used $\sigma_0 = 1.0$ cm$^{-1}$ and $p_0 = 2.0$ for the image prior model.

Figure 13 contains reconstructed images of the absorption coefficient in the measurement plane. Figure 13(a) shows the reconstruction obtained using two complex valued calibration coefficients; Figure 13(b) shows the reconstruction obtained when only a single complex calibration coefficient was used (i.e. the two coefficients were assumed equal); Figure 13(c) shows the reconstruction obtained with a single real valued calibration coefficient; and finally Figure 13(d) assumed all calibration coefficients to be 1. The reconstruction of Fig. 13(a) used the most accurate model and also produced a reconstruction that appears to be more accurate in shape than Fig. 13(b,c). Generally, the elliptical shape of the reconstruction in Fig. 13(c) appears to be the least accurate. Most importantly, Fig. 13(d) shows that reconstruction without estimation of the calibration coefficients was not possible.

## 5. Conclusions

We have formulated the Bayesian optical diffusion tomography with the source-detector parameter estimation problem and proposed an efficient optimization scheme. Our algorithm does not require any prior calibration, and it estimates coupling coefficients successfully with only a small amount of additional computation. Simulation and experimental results show that images can be reconstructed along with the accurate estimation of the coupling coefficients.

## 6. Acknowledgments

## References

1. S. R. Arridge, "Optical tomography in medical imaging," *Inverse Problems* **15**, R41–R93 (1999).

2. J. C. Ye, K. J. Webb, C. A. Bouman, and R. P. Millane, "Optical diffusion tomography using iterative coordinate descent optimization in a Bayesian framework," *J. Opt. Soc. Am. A* **16**, 2400–2412 (1999).

3. J. C. Ye, C. A. Bouman, K. J. Webb, and R. P. Millane, "Nonlinear multigrid algorithms for Bayesian optical diffusion tomography," *IEEE Trans. on Image Process.* **10**, 909–922 (2001).

4. S. S. Saquib, K. M. Hanson, and G. S. Cunningham, "Model-based image reconstruction from time-resolved diffusion data," in *Medical Imaging: Image Processing, Proc. SPIE*, vol. 3034, 369–380, (Newport Beach, CA) (1997).

5. S. R. Arridge and M. Schweiger, "A gradient-based optimisation scheme for optical tomography," *Optics Express* **2**, 213–226 (1998).

6. A. H. Hielscher, A. D. Klose, and K. M. Hanson, "Gradient-based iterative image reconstruction scheme for time-resolved optical tomography," *IEEE Trans. on Medical Imag.* **18**, 262–271 (1999).

7. D. Boas, T. Gaudette, and S. Arridge, "Simultaneous imaging and optode calibration with diffuse optical tomography," *Opt. Express* **8**, 263–270 (2001).

8. H. Jiang, K. Paulsen, and U. Osterberg, "Optical image reconstruction using dc data: simulations and experiments," *Phys. Med. Biol.* **41**, 1483–1498 (1996).

9. H. Jiang, K. Paulsen, U. Osterberg, and M. Patterson, "Improved continuous light diffusion imaging in single- and multi-target tissue-like phantoms," *Phys. Med. Biol.* **43**, 675–693 (1998).

10. B. W. Pogue, S. P. Poplack, T. O. McBride, W. A. Wells, K. S. Osterman, U. L. Osterberg, and K. D. Paulsen, "Quantitavie hemoglobin tomography with diffuse near-infrared spectroscopy: pilot results in the breast," *Radiology* **218**, 261–266 (2001).

11. B. W. Pogue, C. Willscher, T. O. McBride, U. L. Osterberg, and K. D. Paulsen, "Constrast-detail analysis for detection and characterization with near-infrared diffuse tomography," *Med. Phys.* **27**, 2693–2700 (2000).

12. T. O. McBride, B. W. Pogue, S. Poplack, S. Soho, W. A. Wells, S. Jiang, U. Osterberg, and K. D. Paulsen, "Multispectral near-infrared tomography: a case study in compensating for water and lipid content in hemoglobin imaging of the breast," *Journal of Biomed. Optics* **7**, 72–79 (2002).

13. N. Iftimia and H. Jiang, "Quantitative optical image reconstructions of turbid media by use of direct-current measurements," *Appl. Opt.* **39**, 5256–5261 (2000).

14. A. B. Milstein, S. Oh, J. S. Reynolds, K. J. Webb, C. A. Bouman, and R. P. Millane, "Three-dimensional Bayesian optical diffusion tomography using experimental data," *Opt. Lett.* **27**, 95–97 (2002).

15. J. J. Duderstadt and L. J. Hamilton, *Nuclear Reactor Analysis*, Wiley, New York (1976).

16. A. Ishimaru, *Wave Propagation and Scattering in Random Media*, vol. 1, Academic Press, New York (1978).

17. J. C. Ye, K. J. Webb, R. P. Millane, and T. J. Downar, "Modified distorted Born iterative method with an approximate Fréchet derivative for optical diffusion tomography," *J. Opt. Soc. Am. A* **16**, 1814–1826 (1999).

18. L. E. Baum and T. Petrie, "Statistical inference for probabilistic functions of finite state Markov chains," *Ann. Math. Statistics* **37**, 1554–1563 (1966).

19. S. Geman and D. McClure, "Statistical methods for tomographic image reconstruction," *Bull. Int. Stat. Inst.* **LII-4**, 5–21 (1987).

20. S. S. Saquib, C. A. Bouman, and K. Sauer, "ML parameter estimation for Markov random fields with applications to Bayesian tomography," *IEEE Trans. on Image Process.* **7**, 1029–1044 (1998).

21. A. Mohammad-Djafari, "On the estimation of hyperparameters in Bayesian approach of solving inverse problems," in *Proc. of IEEE Int'l Conf. on Acoust., Speech and Sig. Proc.*, 495–498, (Minneapolis, Minnesota), April 27-30 1993.

22. A. Mohammad-Djafari, "Joint estimation of parameters and hyperparameters in a Bayesian approach of solving inverse problems," in *Proc. of IEEE Int'l Conf. on Image Proc.*, vol. II, 473–476, (Lausanne, Switzerland), September 16-19 1996.

23. K. Lange, "An overview of Bayesian methods in image reconstruction," in *Proc. of the SPIE Conference on Digital Image Synthesis and Inverse Optics*, vol. SPIE-1351, 270–287, (San Diego, CA), 1990.

24. C. A. Bouman and K. Sauer, "A generalized Gaussian image model for edge-preserving MAP estimation," *IEEE Trans. on Image Process.* **2**, 296–310 (1993).

25. S. R. Arridge, "Photon-measurement density functions. Part 1: Analytical forms," *Appl. Optics* **34**, 7395–7409 (1995).

Fig. 1. Pseudo-code specification for (a) the overall optimization procedure and (b) the image update by one ICD scan.

Fig. 2. Isosurface plots (at 0.04 cm$^{-1}$ for $\mu_a$, and 0.02 cm for $D$) for $\mu_a$ (left column) and $D$ (right column) for Phantom A: (a,b) original tissue phantom, (c,d) reconstructions with source-detector calibration, (e,f) reconstructions using the correct weights, (g,h) reconstructions without calibration.

Fig. 3. Cross-sections through the centers of the inhomogeneities (z=0.5 cm for $\mu_a$, z=1.5 cm for $D$) for $\mu_a$ (left column) and $D$ (right column) of Phantom A: (a,b) original tissue phantom, (c,d) reconstructions with source-detector calibration, (e,f) reconstructions using the correct weights, (g,h) reconstructions without calibration.

Fig. 4. Isosurface plots (at 0.04 cm$^{-1}$ for $\mu_a$, and 0.02 cm for $D$) for $\mu_a$ (left column) and $D$ (right column) for Phantom B: (a,b) original tissue phantom, (c,d) reconstructions with source-detector calibration, (e,f) reconstructions using the correct weights, (g,h) reconstructions without calibration.

Fig. 5. Cross-sections through the centers of the inhomogeneities (z=0.0 cm for $\mu_a$, z=0.25 cm for $D$) for $\mu_a$ (left column) and $D$ (right column) of Phantom B: (a,b) original tissue phantom, (c,d) reconstructions with source-detector calibration, (e,f) reconstructions using the correct weights, (g,h) reconstructions without calibration.

Fig. 6. (a) Locations of sources and detectors, (b) Several levels of boundaries: zero-flux boundary, physical boundary, source-detector boundary, and imaging boundary, from the outer boundary.

Fig. 7. (a) Source/detector coupling coefficients used in the simulations. The estimation error of coupling coefficients for (b) Phantom A and (c) Phantom B after 30 iterations. Note that the scale of (b) and (c) is 10 times of that of (a).

Fig. 8. The normalized root mean square error between the phantom and the reconstructed images for (a) Phantom A and (b) Phantom B.

Fig. 9. (a) RMS error in the estimated coupling coefficients versus iteration. (b) Convergence of coupling coefficients for Group 1 (—) and Group 2 (- - -) for Phantom B.

Fig. 10. Image NRMSE comparison between the reconstruction with coupling coefficient calibration and the reconstruction with coupling coefficients fixed to $1 + 0i$, for various standard deviations of coupling coefficients. Images were obtained after 30 iterations.

Fig. 11. Cross-sections of the reconstructed images through the centers of the inhomo-geneities (z=0.5 cm for $\mu_a$, z=1.5 cm for $D$) : for $\sigma_{\text{coeff}} = 0.02$ for (a) $\mu_a$ and (b) $D$, and for $\sigma_{\text{coeff}} = 0.04$ for (c) $\mu_a$ and (d) $D$.

Fig. 12. (a) Culture flask with the absorbing cylinder embedded in a scattering Intralipid solution. (b) Schematic diagram of the apparatus used to collect data.

Fig. 13. Cross-sections for reconstructed images of an absorbing cylinder with (a) two complex valued calibration coefficients, (b) a single complex calibration coefficient, (c) a single real calibration coefficient, and (d) all calibration coefficients assumed to be 1.

main  {

    1. Initialize $\hat{x}$ with a background absorption and diffusion coefficient estimate.

    2. Repeat until converged: {

        (a)  $\hat{\alpha} \leftarrow \dfrac{1}{P} \parallel y - f(\hat{x}, \hat{s}, \hat{d}) \parallel^2_{\Lambda}$                                                Eq.(17)

        (b)  $\hat{s}_k \leftarrow \dfrac{[\; \mathrm{diag}(\hat{d})\; \Phi_k^{(s)}(\hat{x})\;]^H \Lambda_k^{(s)}\; y}{\parallel \mathrm{diag}(\hat{d})\; \Phi_k^{(s)}(\hat{x}) \parallel^2_{\Lambda_k^{(s)}}}$      $k = 1, 2, \ldots, K$            Eq.(18)

        (c)  $\hat{d}_m \leftarrow \dfrac{[\; \mathrm{diag}(\hat{s})\; \Phi_m^{(d)}(\hat{x})\;]^H \Lambda_m^{(d)}\; y}{\parallel \mathrm{diag}(\hat{s})\; \Phi_m^{(d)}(\hat{x}) \parallel^2_{\Lambda_m^{(d)}}}$      $m = 1, 2, \ldots, M$         Eq.(19)

        (d)  $\hat{x} \leftarrow ICD\_update_x \left\{ c(x, \hat{s}, \hat{d}, \hat{\alpha}), \hat{x} \right\}$                                   Eq.(16)

    }

}

(a)

---

$ICD\_update_x \left\{ c(x, \hat{s}, \hat{d}, \hat{\alpha}), \hat{x} \right\}$  {

    1. Compute $\phi_k(\,\cdot\,; \hat{x})$, $k = 1, 2, \cdots, K$ and $g(b_m, \,\cdot\,; \hat{x})$, $m = 1, 2, \cdots, M$.

    2. For $u = 0, 1$,

        For $i = 1, \ldots, N$ (in random order), {

        (a) Compute $[f'(\hat{x}, \hat{s}, \hat{d})]_{*(uN+i)}$ with (24)-(26).

        (b) Update $x_{uN+i}$, as described by Ye, *et al.*[2]

$$\hat{x}_{uN+i} \leftarrow \arg \min_{x_{uN+i} \geq 0} \left\{ \frac{1}{\hat{\alpha}} \left\| y - f(\hat{x}, \hat{s}, \hat{d}) - [f'(\hat{x}, \hat{s}, \hat{d})]_{*(uN+i)} \, (x_{uN+i} - \hat{x}_{uN+i}) \right\|^2_{\Lambda} \right.$$
$$\left. + \frac{1}{p_u \sigma^{p_u}} \sum_{j \in \mathcal{N}_i} b_{u, i-j} |x_{uN+i} - \hat{x}_{uN+j}|^{p_u} \right\} \qquad \text{Eq.(23)}$$

        }

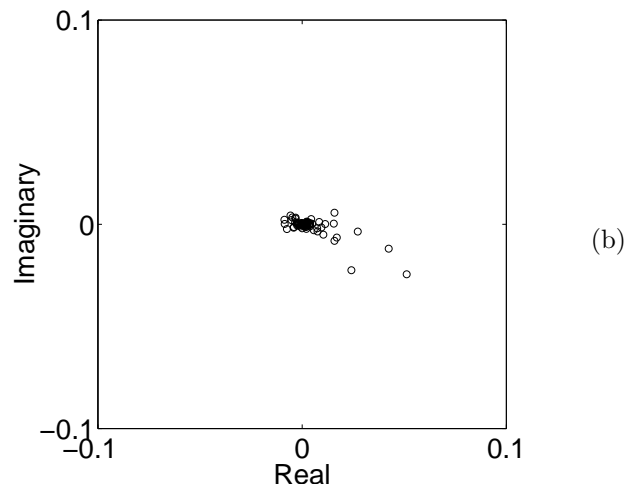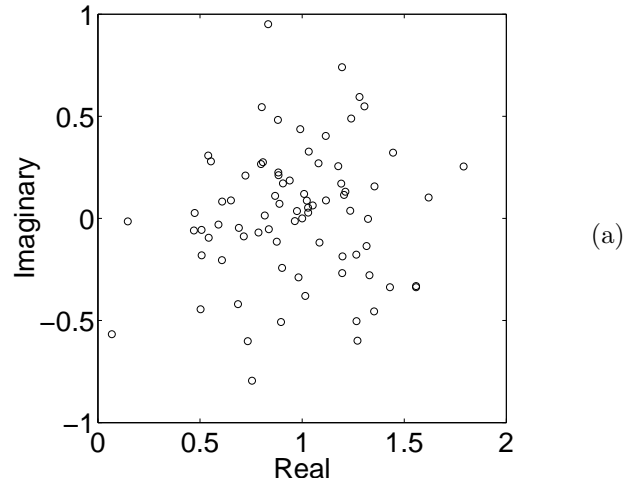    3. Return $\hat{x}$.

}

(b)

Figure 1 (S. Oh. *et al.*)
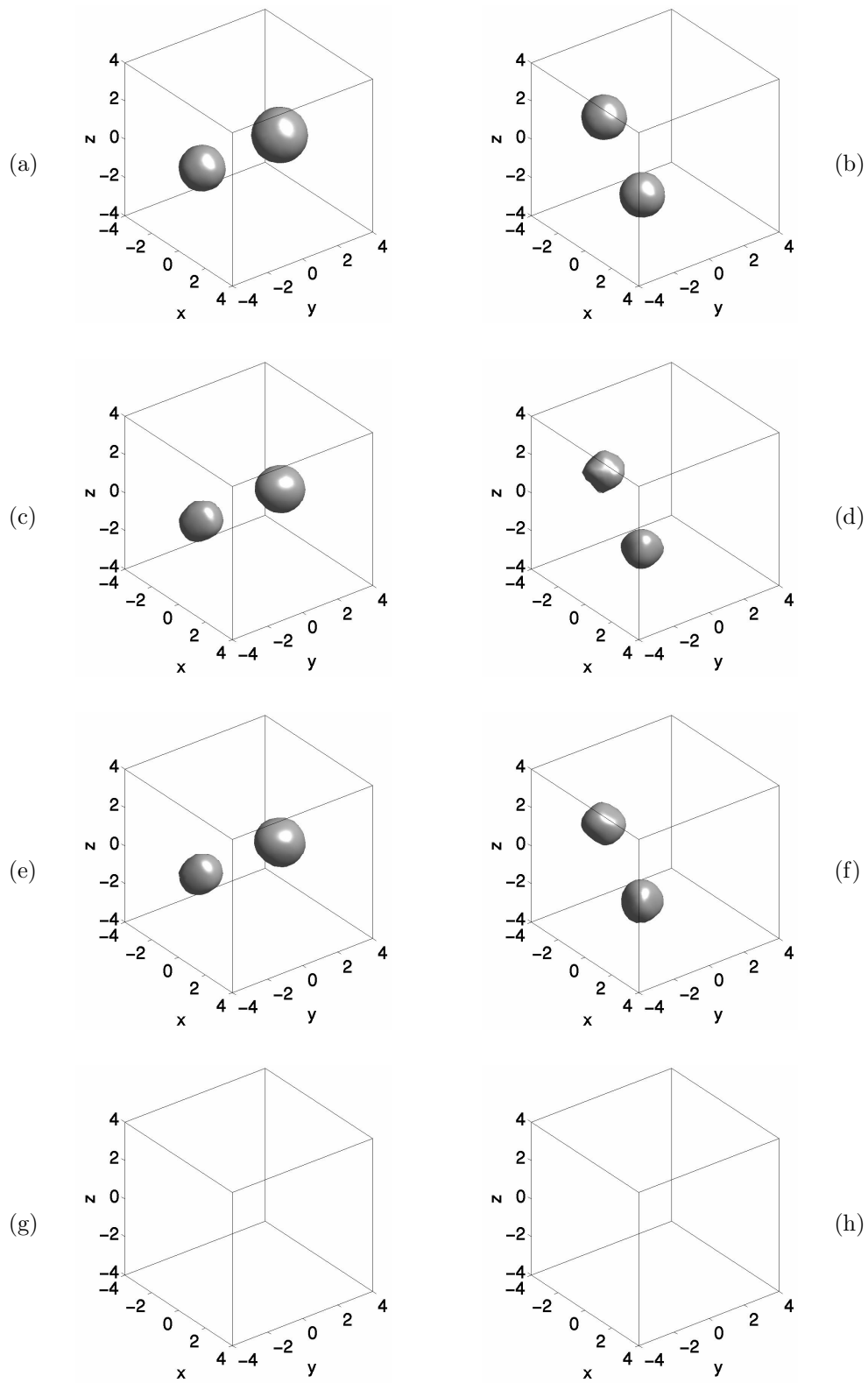
(a)

(b)

(c)

(d)

(e)

(f)

(g)

(h)

Figure 2 (S. Oh. *et al.*)

25

(a)

(b)

(c)

(d)

(e)

(f)

(g)

(h)

Figure 3 (S. Oh. *et al.*)

26

(a)

(b)

(c)

(d)

(e)

(f)

(g)

(h)

Figure 4 (S. Oh. *et al.*)

27

(a)   (b)   (c)   (d)   (e)   (f)   (g)   (h)

Figure 5 (S. Oh. *et al.*)

28

● : source
○ : detector

(a)



zero-flux boundary
physical boundary
source-detector boundary
imaging boundary

(b)

Figure 6 (S. Oh. *et al.*)

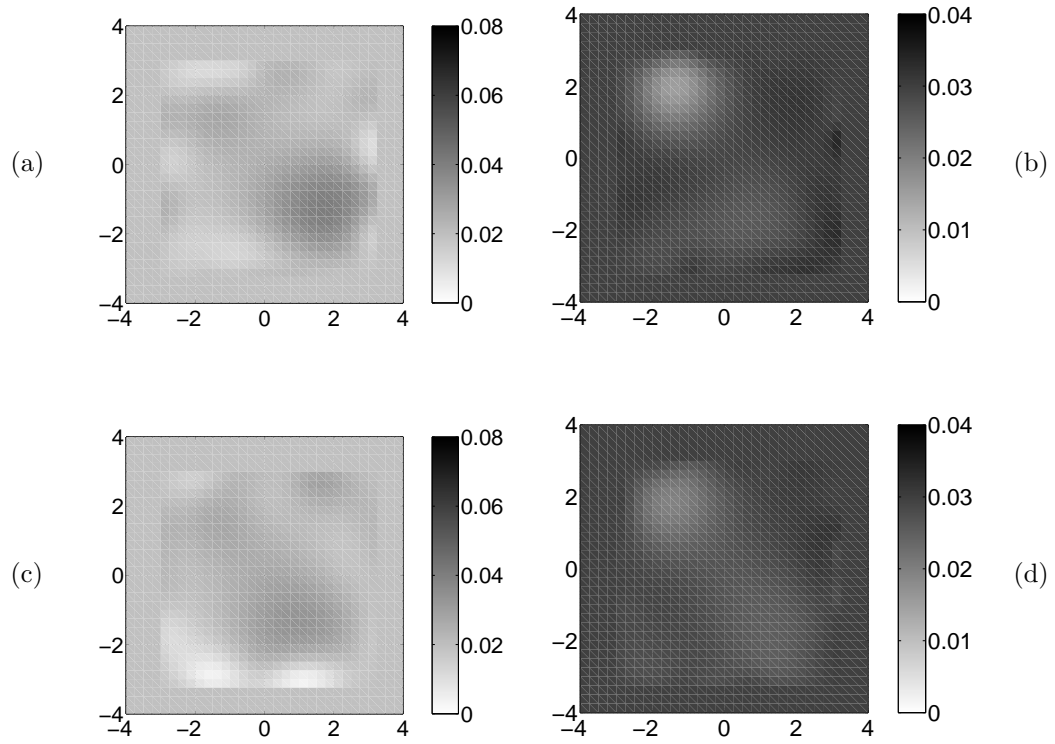(a)

(b)

(c)
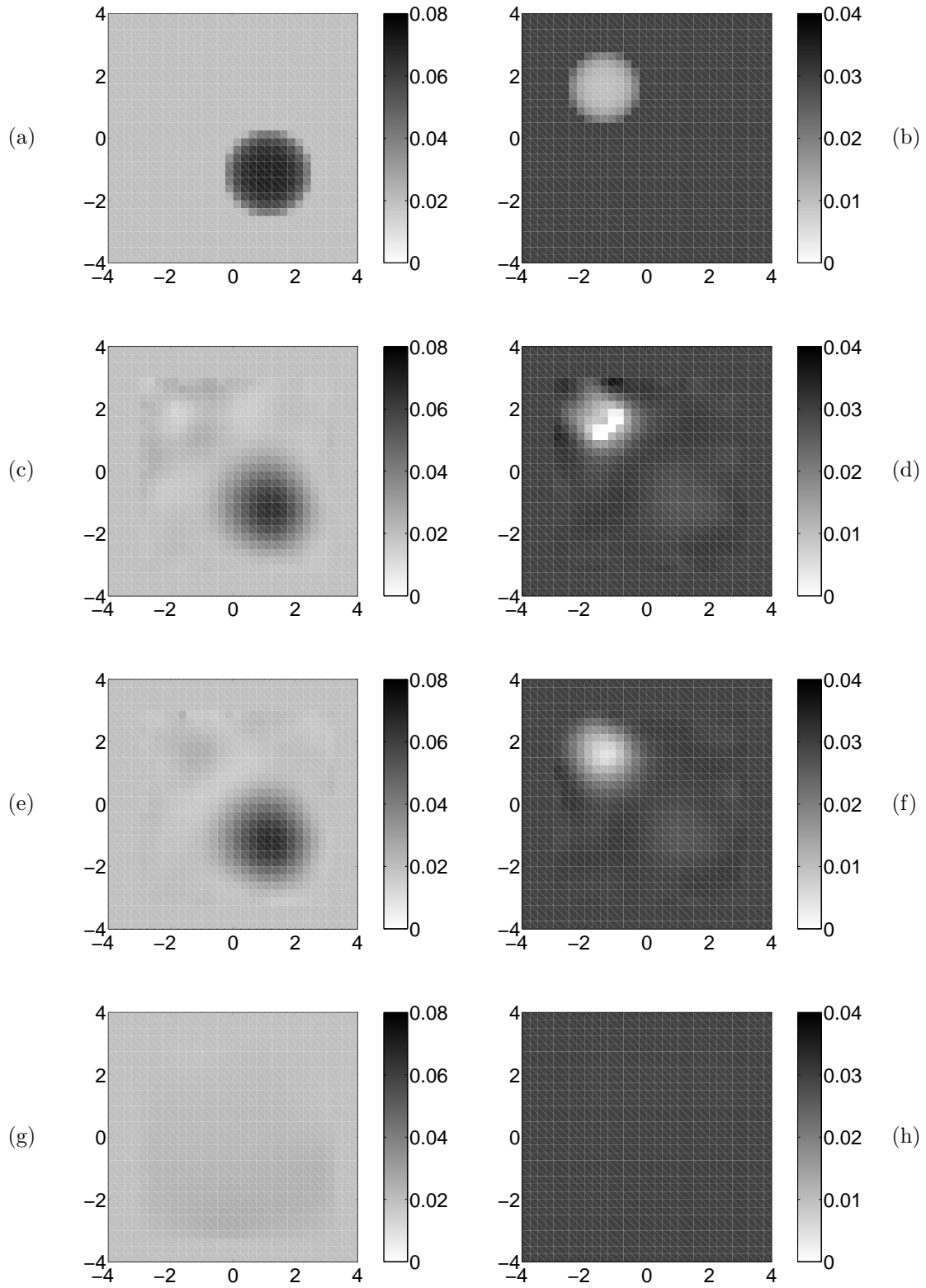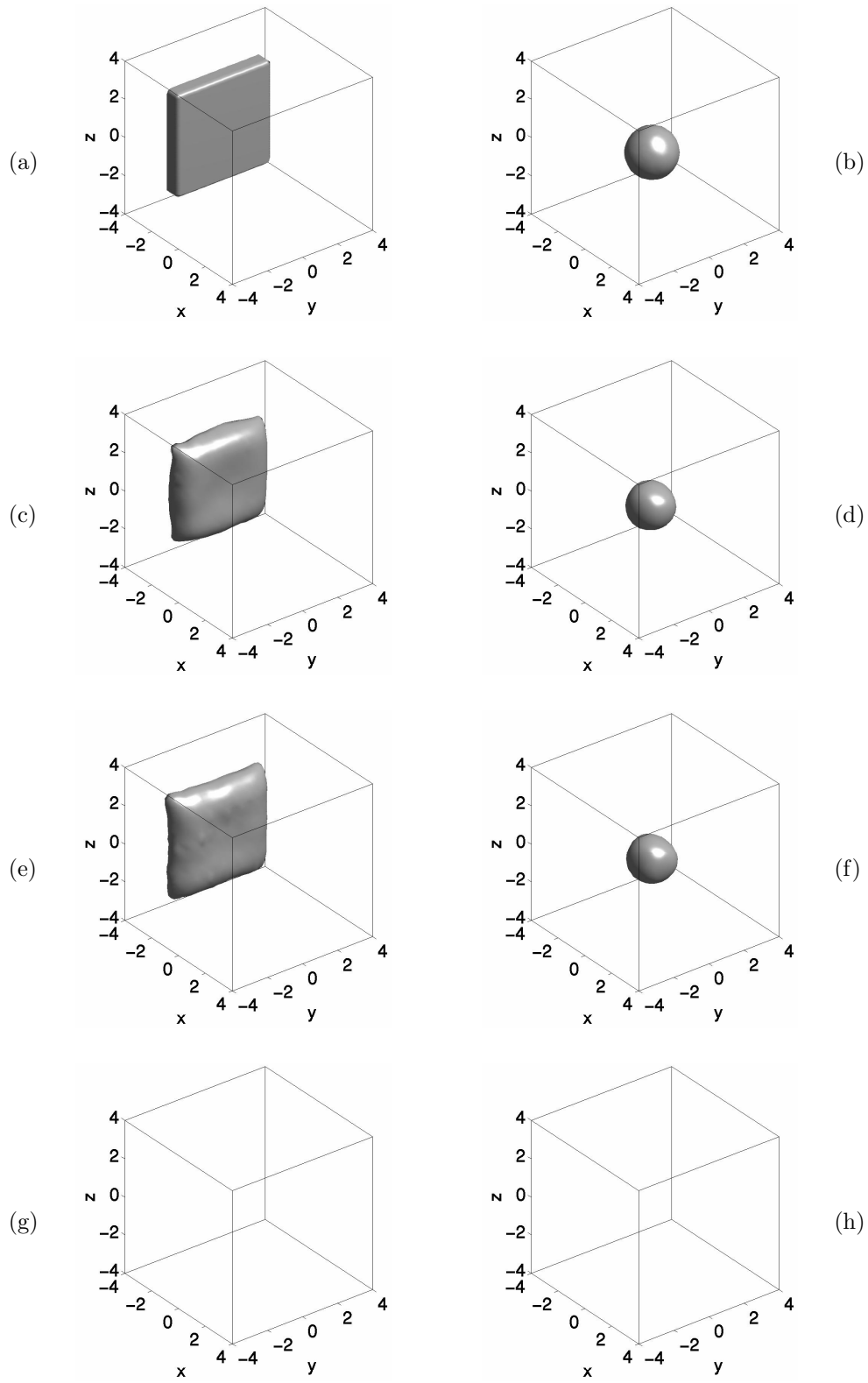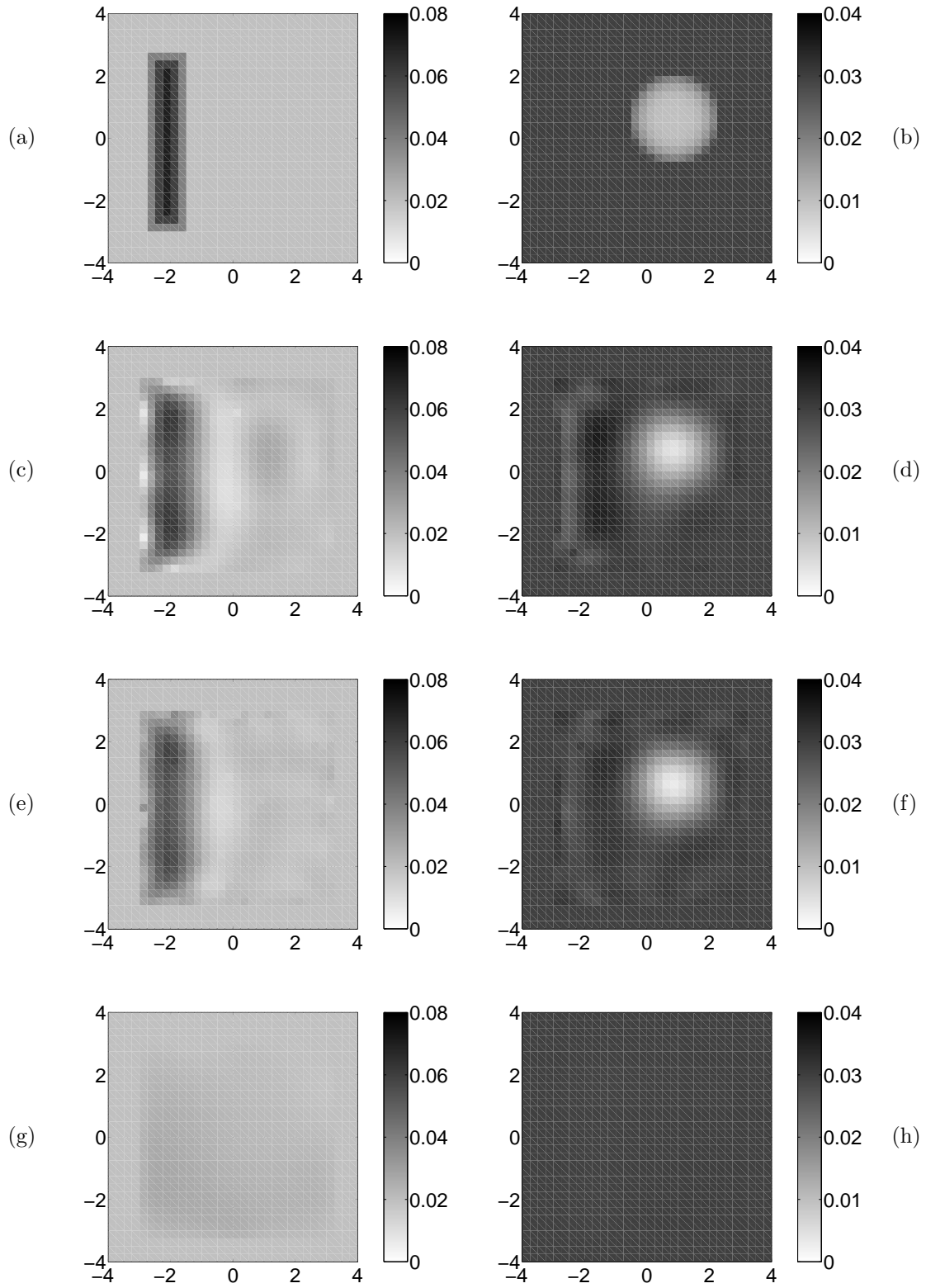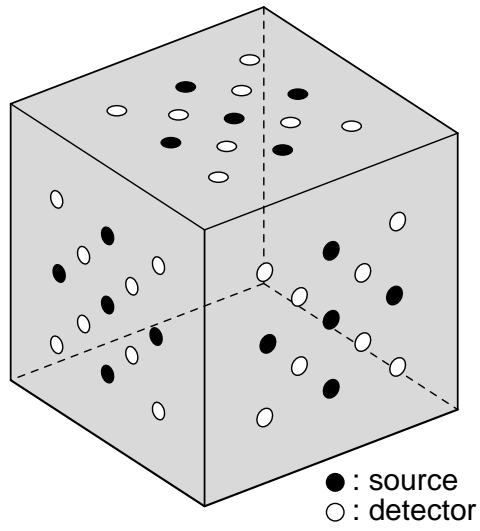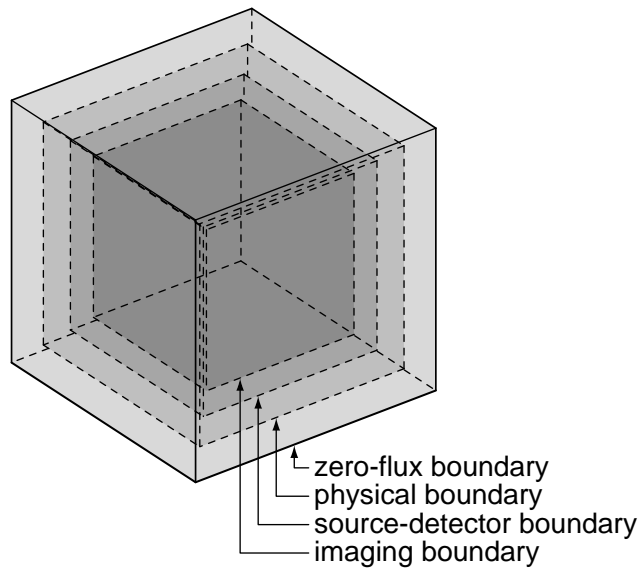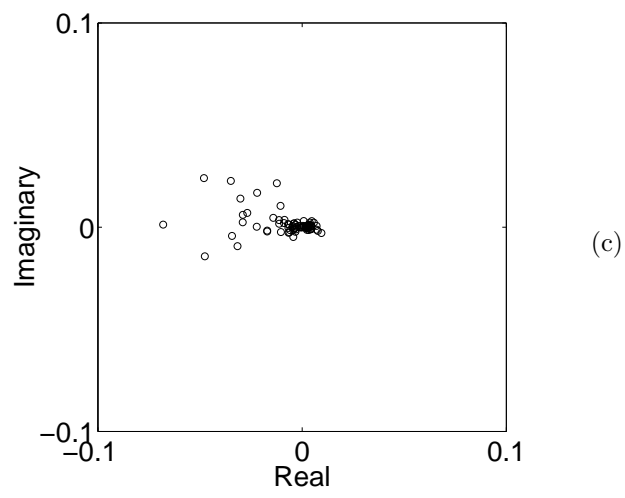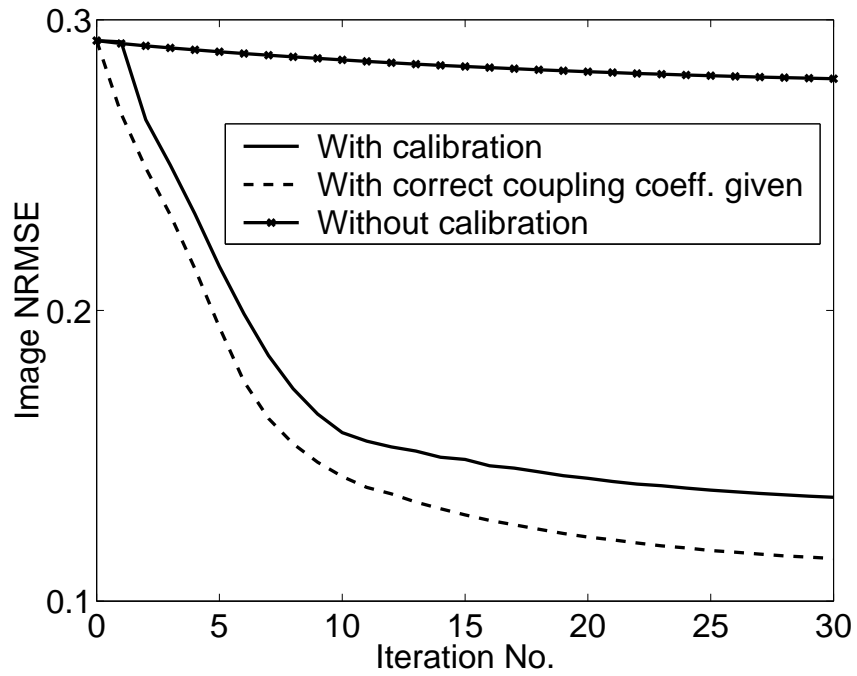
Figure 7 (S. Oh. *et al.*)

(a)
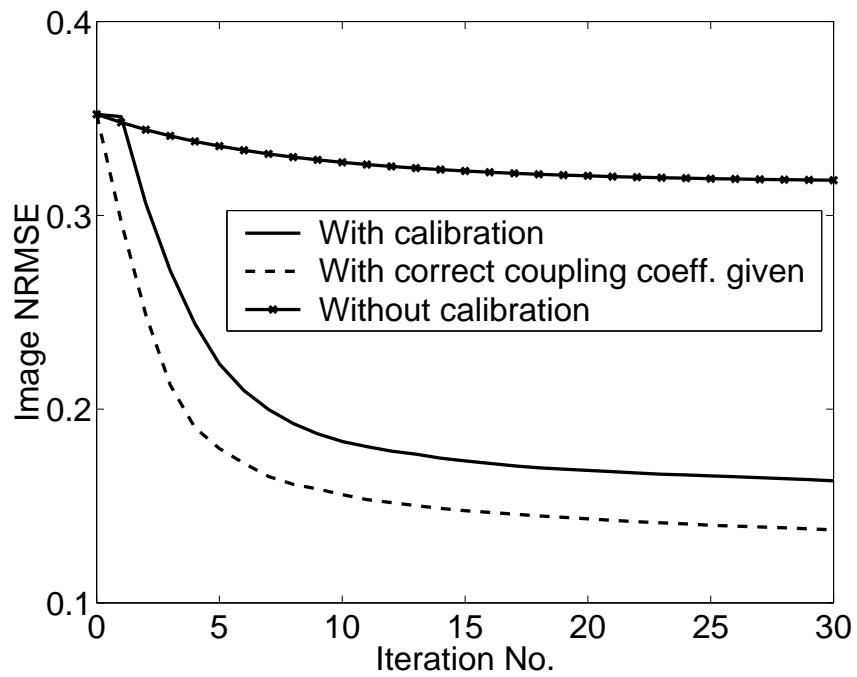


(b)

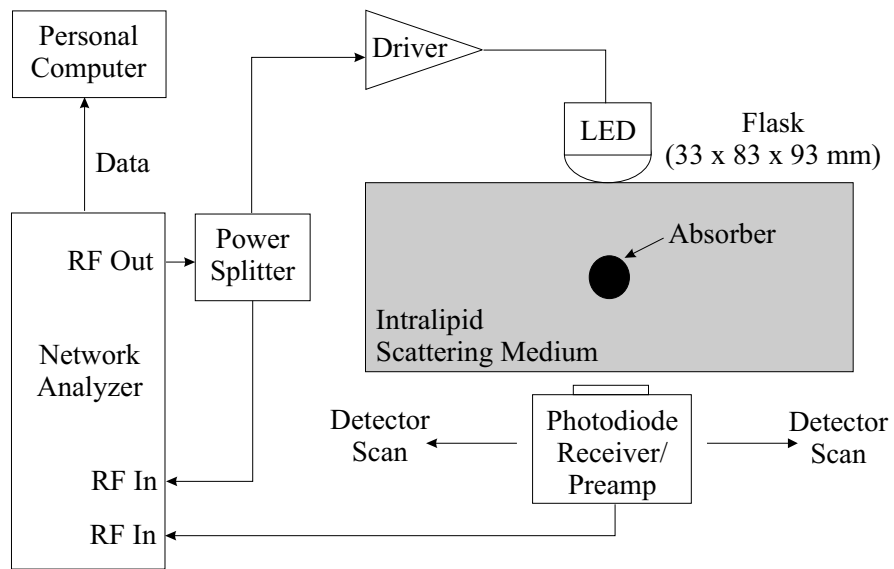Figure 8 (S. Oh. *et al.*)
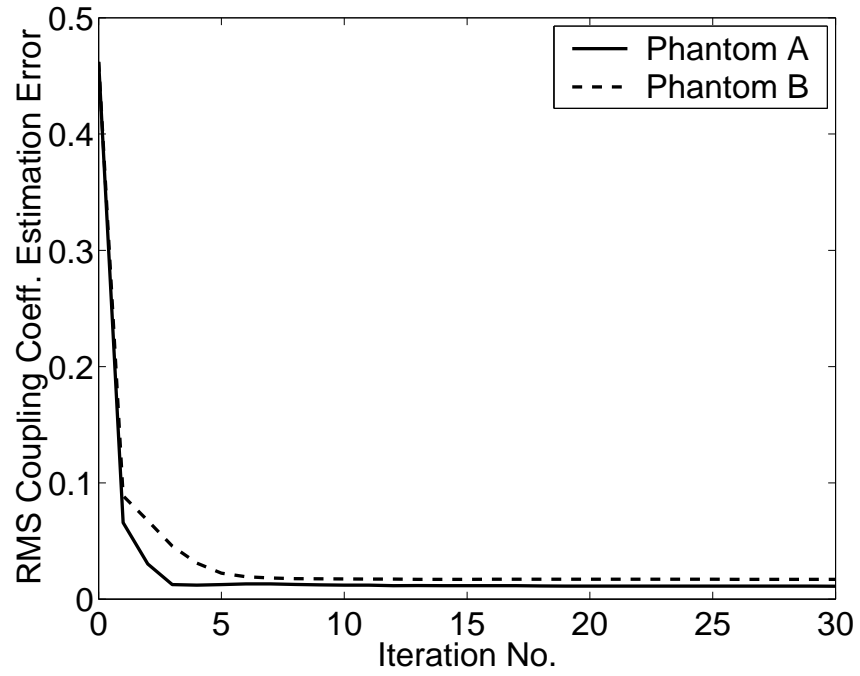
(a)
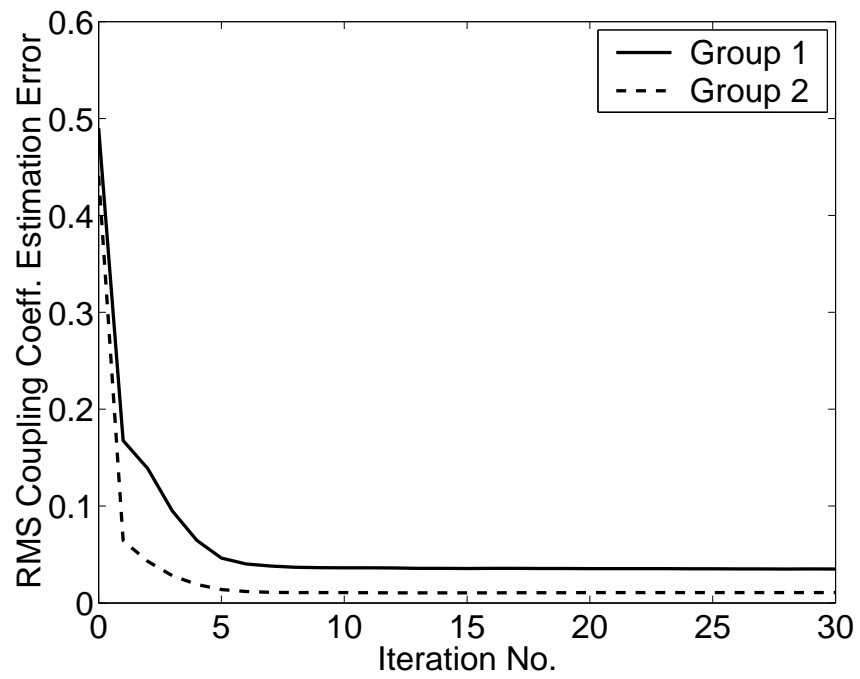


(b)

Figure 9 (S. Oh. *et al.*)

Figure 10 (S. Oh. *et al.*)

(a)

(b)

(c)
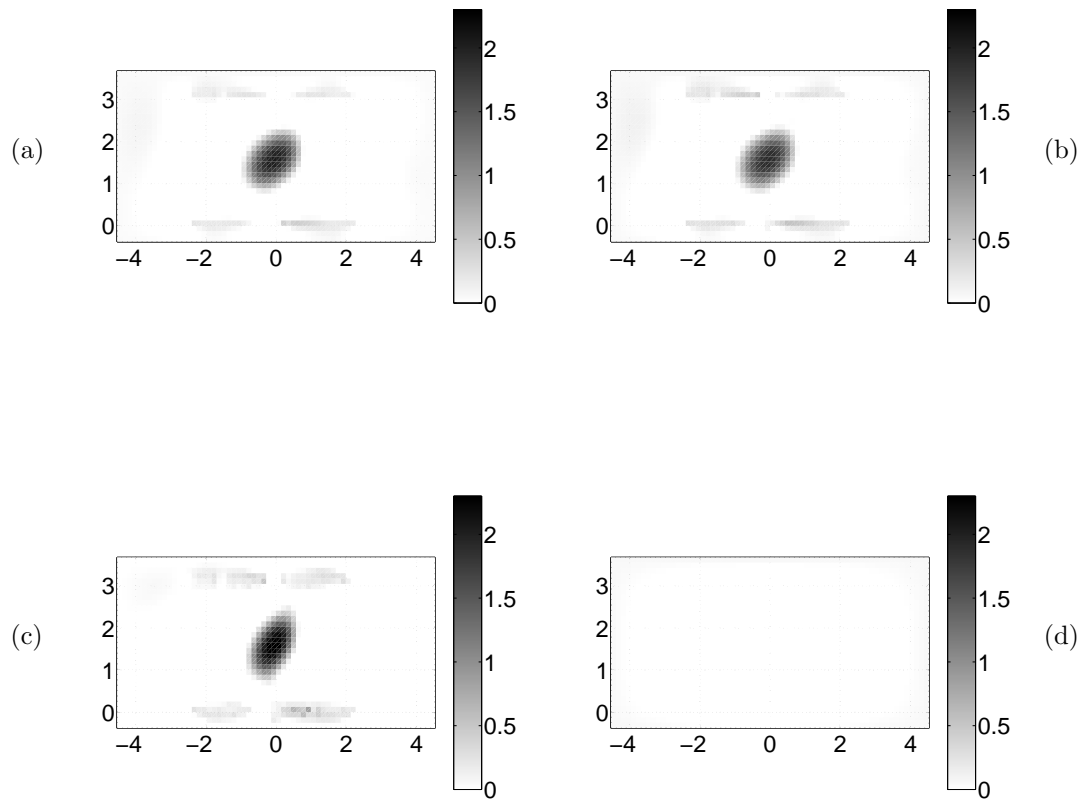
(d)
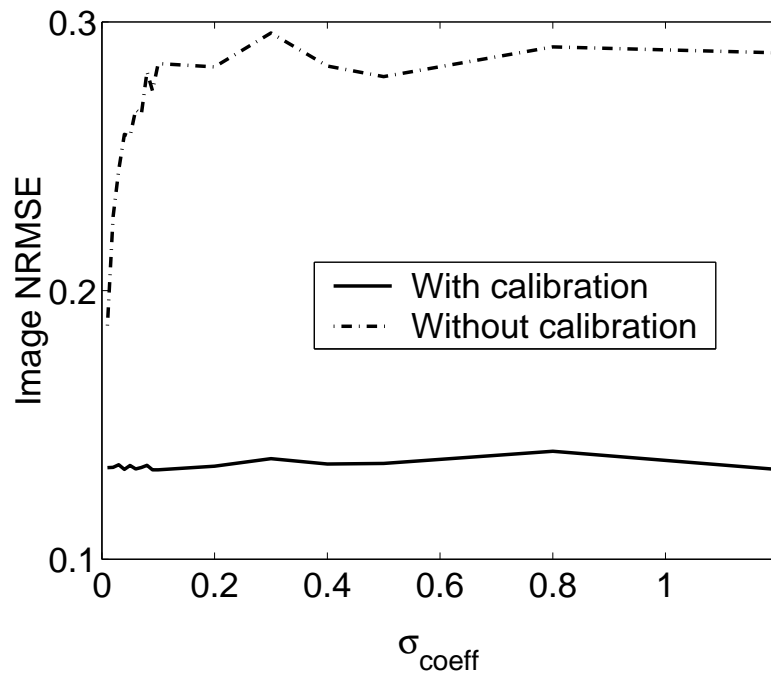
Figure 11 (S. Oh. *et al.*)

(a)



(b)

Figure 12 (S. Oh. *et al.*)

(a)

(b)

(c)

(d)

Figure 13 (S. Oh. *et al.*)